

Article

# A Framework for Soil Salinity Monitoring in Coastal Wetland Reclamation Areas Based on Combined Unmanned Aerial Vehicle (UAV) Data and Satellite Data

Lijian Xie, Xiuli Feng \*, Chi Zhang, Yuyi Dong, Junjie Huang and Junkai Cheng

Department of Geography and Spatial Information Techniques, Ningbo University, Ningbo 315211, China

\* Correspondence: fengxiuli@nbu.edu.cn; Tel.: +86-1342-932-2315

**Abstract:** Soil salinization is one of the most important causes of land degradation and desertification, often threatening land management and sustainable agricultural development. Due to the low resolution of satellites, fine mapping of soil salinity cannot be completed, while high-resolution images from UAVs can only achieve accurate mapping of soil salinity in a small area. Therefore, how to realize fine mapping of salinity on a large scale based on UAV and satellite data is an urgent problem to be solved. Therefore, in this paper, the most relevant spectral variables for soil salinity were firstly determined using Pearson correlation analysis, and then the optimal inversion model was established based on the screened variables. Secondly, the feasibility of correcting satellite data based on UAV data was determined using Pearson correlation analysis and spectral variation trends, and the correction of satellite data was completed using least squares-based polynomial curve fitting for both UAV data and satellite data. Finally, the reflectance received from the vegetated area did not directly reflect the surface reflectance condition, so we used the support vector machine classification method to divide the study area into two categories: bare land and vegetated area, and built a model based on the classification results to realize the advantages of complementing the accurate spectral information of UAV and large-scale satellite spectral data in the study areas. By comparing the modeling inversion results using only satellite data with the inversion results based on optimized satellite data, our method framework could effectively improve the accuracy of soil salinity inversion in large satellite areas by 6–19%. Our method can meet the needs of large-scale accurate mapping, and can provide the necessary means and reference for soil condition monitoring.

**Keywords:** sentinel-2A; unmanned aerial vehicles; soil salinity; classification; inversion



**Citation:** Xie, L.; Feng, X.; Zhang, C.; Dong, Y.; Huang, J.; Cheng, J. A Framework for Soil Salinity Monitoring in Coastal Wetland Reclamation Areas Based on Combined Unmanned Aerial Vehicle (UAV) Data and Satellite Data. *Drones* **2022**, *6*, 257. <https://doi.org/10.3390/drones6090257>

Academic Editor: Fei Liu

Received: 8 August 2022

Accepted: 13 September 2022

Published: 16 September 2022

**Publisher's Note:** MDPI stays neutral with regard to jurisdictional claims in published maps and institutional affiliations.



**Copyright:** © 2022 by the authors. Licensee MDPI, Basel, Switzerland. This article is an open access article distributed under the terms and conditions of the Creative Commons Attribution (CC BY) license (<https://creativecommons.org/licenses/by/4.0/>).

## 1. Introduction

In recent years, the concentration of soluble salts in the surface or near-surface soil layers and their distribution range has increased in some areas due to both natural and anthropogenic factors [1]. This increase in soil salinity poses a serious threat to agricultural activities, vegetation growth, biodiversity, and sustainable development [2–4]. Having up-to-date information on spatial distribution and severity of soil salinity is essential for agricultural management of affected areas. Researchers estimate that about 950 million ha of land are subjected to soil salinization at the global scale and this area is expanding at a speed of  $2.00 \times 10^6$  ha per year [5,6]. High salt concentrations in soils accelerate the process of land degradation and decrease crop yields and agricultural production.

In China in particular, saline soils cover 34 million square kilometers and are unevenly distributed in several regions [7]. Among them, the coastal mud flats along the south coast of Hangzhou Bay are an important reserve resource of wetlands and arable land. Due to the accelerated urbanization, some land resources have been abused, resulting in the reduction of arable land resources. To supplement cultivated land resources, some seabed reclamation areas have been developed. However, the soil type in the initial stage of reclamation is mainly saline-alkali land, which generally requires a long period of soil improvement

before it can be used normally. Hence, accurately, and rapidly obtaining information related to regional soil salinization and its geographical distribution is a prerequisite for the agricultural utilization of salinized soil.

Traditional methods of soil salinity measurement usually rely on costly field soil sample collection and laboratory instrument analysis that make frequent large-scale soil salinity monitoring difficult [8–10]. Because of this, satellite platforms that can provide massive quantities of information over large spatial areas at low cost and at frequent intervals have gradually replaced traditional soil salinity monitoring methods [11,12]. However, satellites also have their own disadvantages, such as fixed orbits and long revisit periods, and satellite data suffer from atmospheric effects and especially from low spatial resolution. This makes it difficult to perform high-precision, real-time inversions in the field using satellite monitoring [13].

As a new remote sensing platform, UAVs have the advantages of high time efficiency, high spatial resolution, low altitude flight under clouds, and high mobility, etc. They can quickly and accurately complete the task of monitoring salinity in a given area [14,15]. Compared with satellites, UAVs have shortcomings in monitoring soil salinity on a large scale, however, and are not permitted in certain areas due to privacy concerns. Although an inversion model based on UAV imagery boasts a higher accuracy, satellite remote sensing remains the best source of basic imagery when acquiring information over a large region [16]. Therefore, combining the high spatial resolution of UAV remote sensing with the large-scale monitoring of satellite remote sensing to achieve high-precision and large-scale soil salinity monitoring has become a hot issue in current research.

For saline cultivated land covered with crops, it is impossible to obtain the spectral reflectance of a soil surface directly by the UAV multispectral camera, as would be the case with bare ground. Therefore, to improve the inversion accuracy of soil salt in cultivated land, many studies have introduced the spectral index. Dong et al. developed five soil salinity inversion models for different soil moisture levels (drought levels) to evaluate regional soil salinity conditions based on the canopy response salinity index (CRSI), normalized vegetation index (NDVI), and automatic water extraction index (AWEI) derived from Landsat TM -8 OLI images [17]. Similarly, Wang et al. constructed cubist and partial least square regression (PLSR) models for regional soil salinity inversion using various relevant covariates (e.g., terrain attributes, remotely sensed spectral indices of vegetation and salinity from the landsat8 OLI satellite) on electrical conductivity (EC) [18].

Although remote-sensing-based regression models are sensor dependent since different sensors have distinct spectral channels, performing spectral index analysis operations can effectively improve the sensitivity of the surface observation data to the parameters of an inversion model [19]. However, due to the different sensor parameters of UAV and satellites and the different scales of data acquisition, when applying a model to corrected satellite data, in addition to the errors brought by the correction of satellite data based on UAVs, there can also be a certain instability in the application of the corrected satellite data by a model constructed based on UAV data. Therefore, it is important to find an alternative to integrating UAV and satellite images.

Considering the factors discussed above, in this study the coastal saline soil area on the south coast of Hangzhou Bay was chosen as the study area in which to perform the following: (1) determination of inversion steps for bare soil and vegetated areas based on UAV images and field measurement data, respectively, and selecting the best model; (2) determination of the satellite data correction method based on the relationship between the reflectance and spectral index corresponding to the UAV and satellite images; (3) selection of samples to classify the study area and obtain the distribution range of vegetated and bare soil areas, and the subsequent application of the inversion process and the best inversion model established in the first step to the quality-enhanced satellite data for modeling again to achieve accurate soil salinity inversion over a large area.

The purpose of this paper was to construct an inversion framework based on UAV data and satellite data for accurate mapping of soil salinity in large scale regions. The key

of this study is the selection of inversion variables and the construction of a method to correct satellite data based on UAV data, as well as the verification of the robustness of the constructed soil salinity inversion model based on the classification results. So, the rest of the paper is organized as follows. Section 2 introduces the study area and data sources. In Section 3 we present the proposed method in detail. Section 4 illustrates the experimental results, and in Section 5 the applicability of the method is discussed. Section 6 provides the conclusions.

## 2. Study Area and Data Source

The study area is located in the south coast of Hangzhou Bay (Figure 1a) in the northeastern part of Zhejiang province, China and is connected to the Qiantang River in the west and the East China Sea in the east. Due to the accumulation of inlet sediment in the bay, partly moved southward by wave and tidal dynamics, the south coast of Hangzhou Bay has become one of the largest and most well-developed estuarine tidal flats in the world [20]. The region borders the Yangtze River delta plain and the volcanic hills of southeastern Zhejiang province, and the terrain is dominated by plains and low hills, with a humid subtropical monsoon climate; it has a long summer and a slightly shorter spring and autumn. The average annual sunshine hours are 2038, with an annual sunshine percentage of 47%. Average annual temperature is 16–21 °C and the average annual precipitation is over 1000 mm. Catastrophic weather events in the territory are dominated by water, drought, winds, and tides [21].

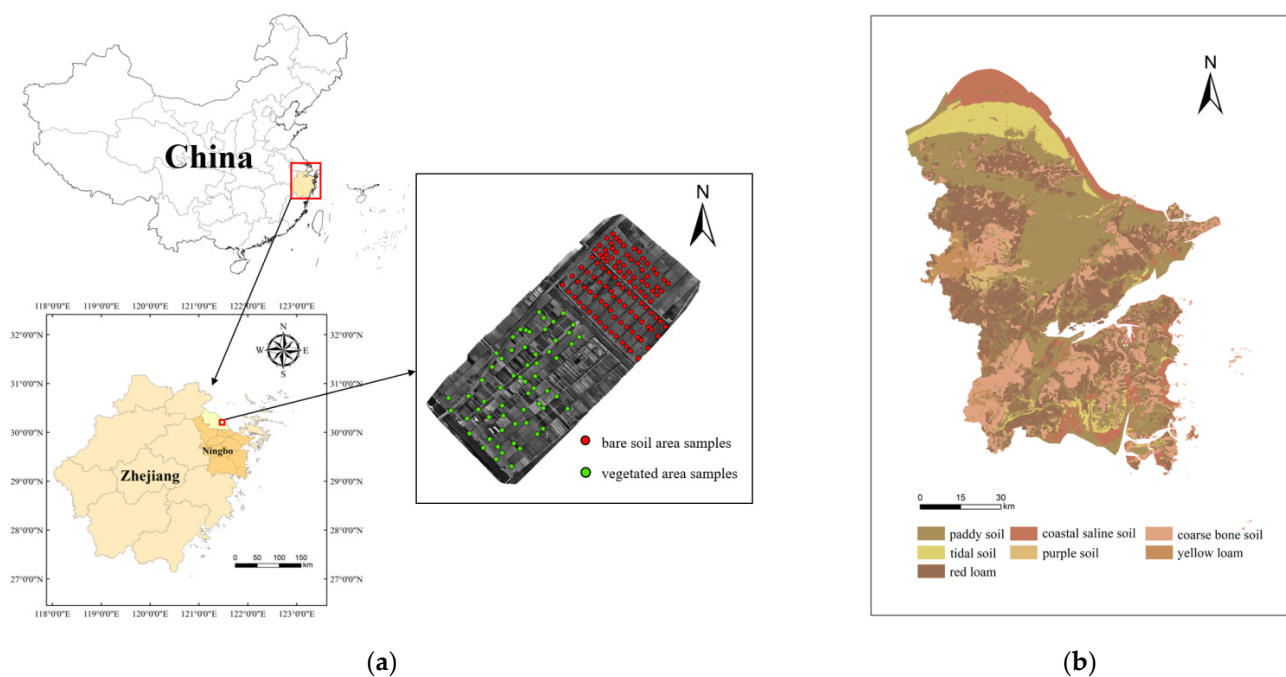


**Figure 1.** (a) The geographical location of the study area; (b) Ningbo soil classification map.

Hangzhou Bay has experienced a rapid expansion of coastal reclamation in recent years to supplement land resources in a manner that can be regarded as a typical case of coastal reclamation in China's rapidly developing regions [22]. As shown in Figure 1b, the soil types from sea to land are, in order, coastal saline soil, tidal soil and paddy soil. The first two have a high salt content and the anthropogenically modified paddy soils have a short soil formation time and are slightly alkaline. Although the cultivated land after reclamation has been transformed by various soil desalination measures, soil desalination is a long process and the problem of soil salinization is still a major factor that affects agricultural production in the region.

### 2.1. Acquisition of Soil Salinity Data

As shown in Figure 1a, the study area covers 3.83 km<sup>2</sup>. In total, 174 soil samples were collected in the study area; each sample was collected from the four corners and the center of the sampling quadrat, with a size of 10 m × 10 m. The geographic coordinates of the sampling sites were obtained using a handheld Trimble Geo Explorer GPS device (Trimble Navigation Ltd., Inc., Sunnyvale, CA, USA), and the sampling was conducted on 14 January 2021, including both bare soil areas yet to be cultivated and vegetated areas covered by crops. Soil sampling was performed at the soil surface (0~10 cm), and physicochemical characteristics such as soil salinity were measured in the laboratory. The soil samples were air-dried and sieved with a 1 mm sieve and mixed with distilled water at a ratio of 1:5 in a flask [23]. The soil salinity was then determined from the linear regression equation derived by predecessors,  $SSC = 2.18EC + 0.727$  [24], where SSC represents the soil salinity content in units of g/kg. The average value of repeated measurements was taken as the measured soil salinity at each sampling point. To ensure the data were as accurate and representative as possible, 6 anomalous outlier samples were removed, leaving 168 for use in the study (Table 1). Figure 2 shows the spatial distribution of soil salinity content. The maximum value of soil salinity content in the study area is 7.437 g/kg, and the minimum value is 0.541 g/kg.

**Table 1.** Salinization classification and sample distribution.

Soil Salinity Level	Non-Saline	Mild Salinization	Moderate Salinization	Severe Salinization	Saline Soil
Salt content */(g·kg <sup>-1</sup> )	<1.0	1.0–2.0	2.0–4.0	4.0–6.0	>6.0
Number of samples (ratio)	38(23%)	50 (30%)	53 (31%)	22 (13%)	5 (3%)

Note: \* based on Bao, 2010 [25].

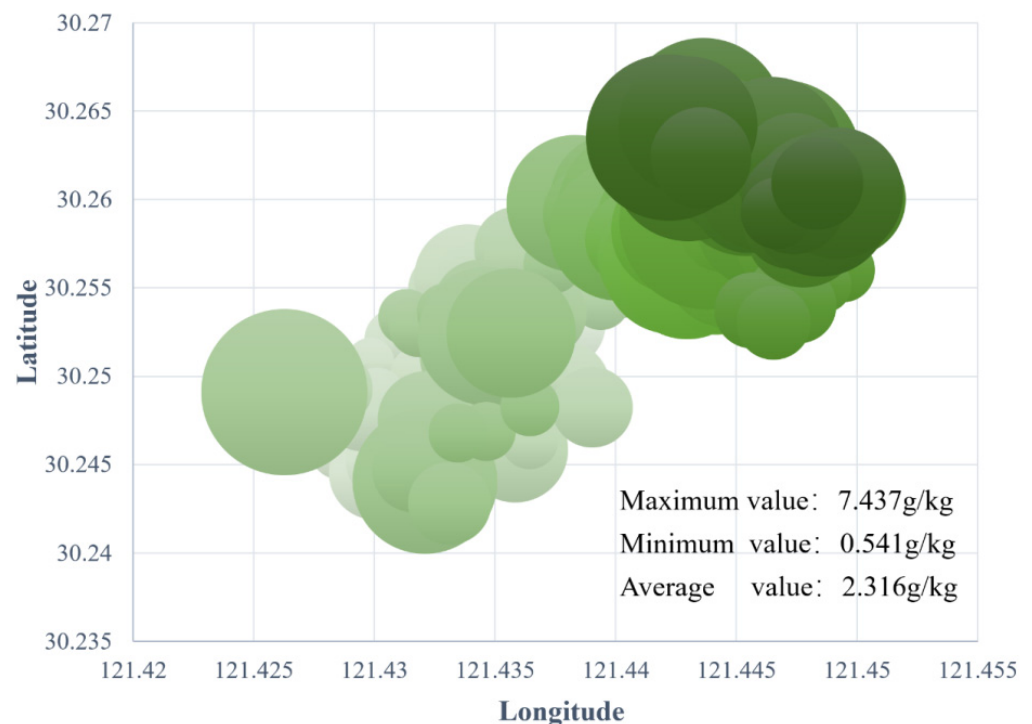


**Figure 2.** Soil salinity content spatial distribution map.

### 2.2. Acquisition and Processing of UAV Imagery

The platform used for remote sensing was the XMISSION multi-rotor UAV produced by XAG, which is equipped with an XCam Multi-Spectrum agricultural multispectral

camera. This camera can receive a total of four bands of information, green (G), red (R), red edge (R-edge), and near infrared (NIR) with wavelengths of 550 nm, 660 nm, 735 nm, and 790 nm (Table 2). The data were collected on 14 January 2021, from 11 a.m. to 15 p.m. in clear, cloudless weather. The flight altitude was set to 110 m, the heading overlap rate and side overlap rate were both 70%, white reflectors were arranged on the ground for radiation correction, and an appropriate number of ground control points was selected. The acquired images were synthesized using Pix4Dmapper software (Pix4D, S.A., Prilly, Switzerland), and geographic alignment, radiometric correction, and geometric correction were performed in ENVI 5.3 (Exelis Visual Information Solutions, Inc., Boulder, CO, USA) to obtain multispectral image data with a resolution of 0.13 m.

**Table 2.** Band information of the S2A data and UAV data.

Sentinel-2A Data			UAV Data		
Bands	Central Wavelength (nm)	Resolution (m)	Bands	Central Wavelength (nm)	Resolution (m)
B3-Green	560	10	Green	550	0.13
B4-Red	665	10	Red	660	0.13
B6-Vegetation red edge	740	20	Red Edge	735	0.13
B7-Vegetation red edge	783	20	Near-infrared	790	0.13

### 2.3. Acquisition and Processing of Sentinel-2A Satellite Data

Maintaining similar dates for field sampling, UAV images, and satellite images is required for accurate soil salinity inversion. The Sentinel-2A products from the website of the European Space Agency (ESA, <http://www.esa.int/> (accessed on 15 January 2021)) were used as satellite remote sensing image data, and the multispectral image was acquired at a similar time to the UAV image. The Sentinel-2A satellite has 13 spectral bands, from visible to shortwave-infrared bands, and three spatial resolutions, including 10 m (four bands), 20 m (six bands), and 60 m (three bands) ground resolution, which can monitor the growth, and obtain information on crop planting and land use changes. First, radiometric calibration and atmospheric correction were performed using the Sen2cor plug-in released by the ESA. The data were then resampled with Sentinel Application Platform (SNAP) software to generate 10 m spatial resolution images and export the data. Soil salinity inversion was based on differentiated fusion of satellite image and ground spectra. Finally, the images were stitched together using ENVI 5.3 software (Exelis Visual Information Solutions, Inc., Boulder, CO, USA) and cropped using the study area boundary vector file to obtain the Sentinel-2A image of the study area. In order to be consistent with the UAV image bands (Table 2), the B3\B4\B6\B7 bands of the Sentinel-2A images were selected for this study.

### 3. Methods

To improve the accuracy of soil salinity prediction in large-scale regions, we propose a soil salinity inversion framework that combines UAV data and satellite data (Figure 3). The method consists of three parts: correlation analysis between soil salinity and spectral variables to determine sensitive parameters for modeling and inversion; correlation analysis of spectral variables between UAV data and satellite data to determine the feasibility of optimizing satellite data based on UAV data; and using the mask obtained after classification to extract the optimized satellite image vegetation area and bare soil area data for modeling. The key to the research is to determine whether the basic characteristic spectra of UAV images and satellite images are similar. Due to the problem of resolution, satellite data cannot accurately obtain the spectral information of ground objects, and UAV data cannot obtain large-scale regional data due to hardware reasons. To achieve precise acquisition

of large-scale soil salinity, it is thus necessary to use UAV data to correct satellite data so that the spectral variable values of satellite data are more accurate. Therefore, similarity analysis between spectral variables is necessary for establishing the correction of satellite data based on UAV data.

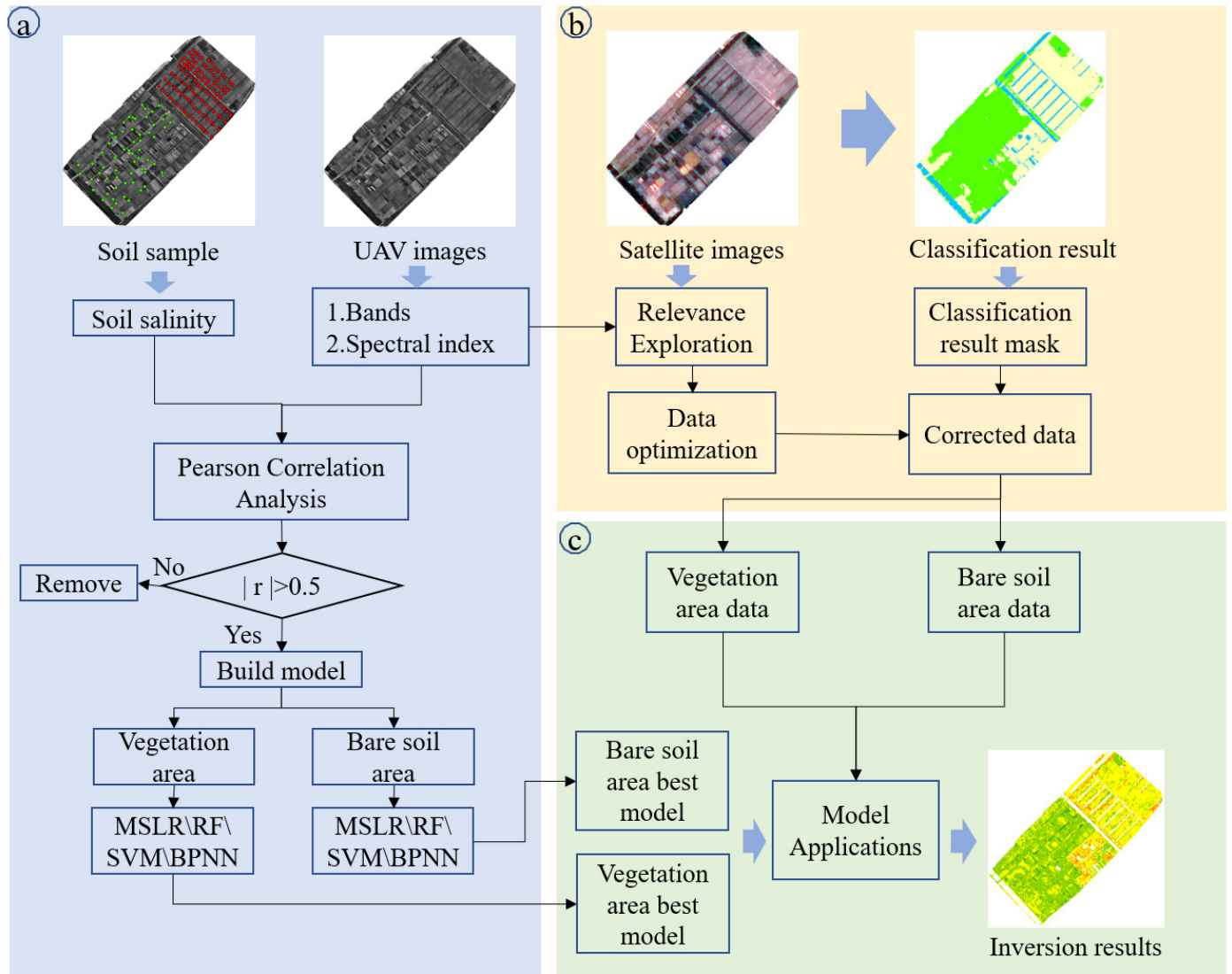


**Figure 3.** The workflow of this study: (a) building a model based on UAV Imagery; (b) correction of satellite data based on UAV data; (c) soil salinity inversion based on corrected data.

To accomplish this, the spectral index was first generated by the band combination operations (arithmetic operations between bands), and all the measured data were subjected to Pearson correlation analysis with the UAV band data and the calculated spectral index. The band or band combination with a larger absolute value of correlation coefficient ( $|r|$ ) was selected as the sensitive band or spectral parameter. Second, according to the relationship between spectral variables, basic characteristic spectra were extracted from UAV and satellite images and normalized as the basic matrix of spectral data. A polynomial fitting function for optimizing Sentinel-2A spectral variables based on UAV was established by numerical regression [26,27]. Finally, the optimal modeling method in the vegetation area and bare soil area established in the first step was used to model the satellite data after polynomial function optimization, and the resulting model was then applied to the vegetation area and bare soil area data extracted by mask to complete the soil salinity inversion.

### 3.1. Soil Salinity Inversion Model Based on UAV Imagery

#### 3.1.1. Filter Sensitive Variables

To filter the sensitive variables appropriate, the reflectance values of the UAV images that correspond to the sampling points in the test area were first extracted by ArcGIS 10.3 (Environmental Systems Research Institute, Inc., Redlands, CA, USA) based on the sample coordinates. The spectral indicators (Table 3) were then generated by combining the bands, and the soil samples and spectral indicators were subjected to Pearson correlation analysis to filter out the sensitive bands and sensitive spectral indicators with correlation coefficients  $|r| > 0.5$ . This process was implemented in Matlab2018a.

**Table 3.** Spectral indicators.

No.	Name	Formula	Reference
1	Green	—	—
2	Red	—	—
3	R-edge	—	—
4	NIR	—	—
5	Salinity index VI (S6)	$(R + NIR)/G$	[28]
6	Intensity Index 1 (INT1)	$(G + R)/2$	[29]
7	Intensity Index 2 (INT2)	$(G + R + NIR)/2$	[29]
8	Salinity Index 1 (SI1)	$0.5 \times (G \times R)$	
9	Salinity Index 2 (SI2)	$(G^2 + R^2 + NIR^2)^{0.5}$	[28]
10	Salinity Index 3 (SI3)	$(G^2 + R^2)^{0.5}$	
11	Salinity index I red-edge 1 (SI1-R-edge)	$(G \times R - edge)^{0.5}$	
12	Salinity index I red-edge 2 (SI2-R-edge)	$(G^2 + R - edge^2 + NIR^2)^{0.5}$	[30]
13	Salinity index I red-edge 3 (SI3-R-edge)	$(G^2 + R - edge^2)^{0.5}$	
14	Salinity Index (SI-T)	$R/NIR$	
15	Ratio Vegetation Index (RVI)	$NIR/G$	[7]
16	difference vegetation index (DVI)	$NIR - R$	
17	difference vegetation index red-edge (DVI-R-edge)	$NIR - R - edge$	[31]
18	Triangle vegetation index (TVI)	$\left(\frac{NIR-R}{NIR+R} + 0.5\right)^{0.5}$	[32]
19	Soil Adjusted Vegetation Index (SAVI)	$(1 + L) \times \frac{NIR-R}{NIR+R+L}, L = 0.5$	[33]
20	Normalized Difference Green Index (NDGI)	$(G - R)/(G + R)$	[34]
21	Simple Ratio (SR)	$NIR/R$	[35]
22	Brightness index (BI)	$(R^2 + NIR^2)^{0.5}$	[36]
23	Normalized Difference Vegetation Index (NDVI)	$(NIR - R)/(R + NIR)$	[7]
24	Normalized Difference Salinity Index (NDSI)	$(R - NIR)/(R + NIR)$	[36]

#### 3.1.2. The Construction of the Optimal Inversion Model

Among the sample data collected, there were 107 samples in the bare land area and 61 samples in the vegetation coverage area. Multiple linear regression (MLR), random forest (RF), support vector machine (SVM), and back propagation neural network (BPNN) modeling methods were used in this paper. MLR, PLSR, SVM, and BPNN were all implemented in Python3.7 using the sklearn library, and Keras2.2.0. The parameters in the model need to be optimized before applying the calibration model, making them so-called “hyperparameters” that have a large impact on the model performance [37]. Therefore, we used a grid search method to optimize the model’s hyperparameters. The prediction performance of different models was evaluated by the method of five-fold cross validation. Here, all measured values were randomly divided into five groups, among which four groups were selected as the training set and the remaining one group was selected as the validation set. Compared with randomly dividing the training set and the validation set, five-fold cross validation increases a model’s reliability [38].

The coefficient of determination ( $R^2$ ), mean absolute error (MAE), and root mean square error (RMSE) were used to evaluate the accuracy of model modeling and validation [31,39–42].  $R^2$  measures how well the model fits the data, and RMSE reflects the

deviation between the observed and predicted values. The closer  $R^2$  was to 1, and the smaller the  $MAE$  and  $RMSE$ , the higher the model accuracy and the better the effect.

$$R^2 = 1 - \frac{\sum_{i=1}^n (y_i - \hat{y}_i)^2}{\sum_{i=1}^n (y_i - \bar{y})^2} \quad (1)$$

$$MAE = \frac{1}{n} \sum_{i=1}^n |y_i - \hat{y}_i| \quad (2)$$

$$RMSE = \sqrt{\frac{1}{n} \sum_{i=1}^n (y_i - \hat{y}_i)^2} \quad (3)$$

where  $y_i$  and  $\hat{y}_i$  are measured and predicted values, respectively.  $\bar{y}$  is the average of observed values,  $n$  is the total number of validation plots.

### 3.2. Data Optimization and Partition Mask Acquisition

#### 3.2.1. Optimizing Satellite Spectral Variables Based on UAV Data

Numerical regression methods usually use polynomial functions to establish correspondences between data so that one set of data is approximated by fitting to another set of data. In this paper, we established the polynomial fitting function for optimizing the Spectral parameters of Sentinel-2A based on UAV regression and then used the fitting function to optimize the Spectral parameters of the Sentinel-2A data. Previously, since UAVs and satellites have different resolutions, the average reflectance of multiple pixels in each band of the UAV image corresponding to the reflectance of one pixel of the Sentinel-2A image was used as a way of exploring the link between them [13]. The regression fit is in polynomial form as follows [26,27,43]:

$$F'_i = p_0 f_i^n + p_1 f_i^{n-1} + p_2 f_i^{n-2} + \dots + p_n \quad (4)$$

where  $p_0, p_1 \dots p_{n-1}$  are spectral optimization parameters,  $p_n$  is the optimization residual,  $F'_i$  is the normalized UAV reflectance and  $f_i$  is the normalized satellite reflectance,  $i$  is the number of spectral reflectance, and  $n$  is the power of the equation.

#### 3.2.2. Acquisition of Mask Data for Salt Inversion

The surface of the study area is usually composed of both vegetation coverage and bare soil. When using all the samples for inversion, since the spectral parameters obtained from the vegetation coverage area are not the actual spectral parameters of the bare soil on the surface, there will be certain errors whether the inversion is performed from spectral variables or spectral indicators. Therefore, in order to improve the soil salinity inversion accuracy of the satellite data, we first classified satellite images to obtain the range of bare soil area and vegetation coverage area, and then established inversion models for these two areas separately. The obtained classification results come from the supervised classification method on ENVI5.3 (Exelis Visual Information Solutions, Inc., Boulder, CO, USA) software.

## 4. Experimental Results and Analysis

### 4.1. Screening of Soil Salinity-Sensitive Bands and Spectral Parameters

#### 4.1.1. Sensitive Bands

The  $|r|$  values between the ground-measured soil salinity and the reflectance in the UAV imagery are shown in Figure 4. The reflectance values in the green, red, red-edge, and near-infrared bands of the UAV images correspond to G, R, R-edge, and NIR, respectively, in the inversion model. The correlations between salinity and reflectance were above 0.5 in both bare soil and vegetated areas. The R-edge band in the bare soil area had the strongest correlation, and the near-infrared band in the vegetation area had the strongest correlation, at 0.6036 and 0.7056, respectively.

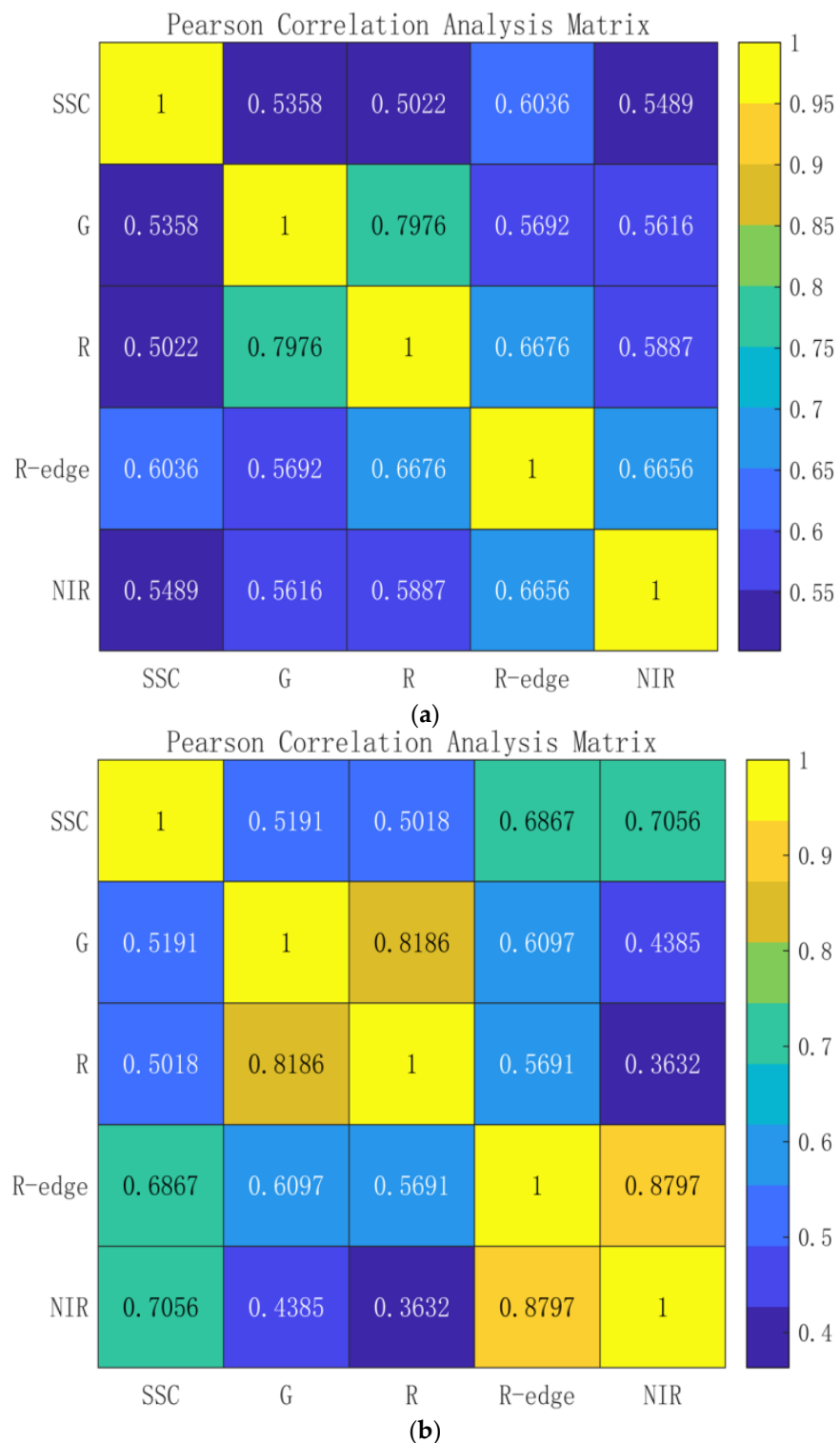
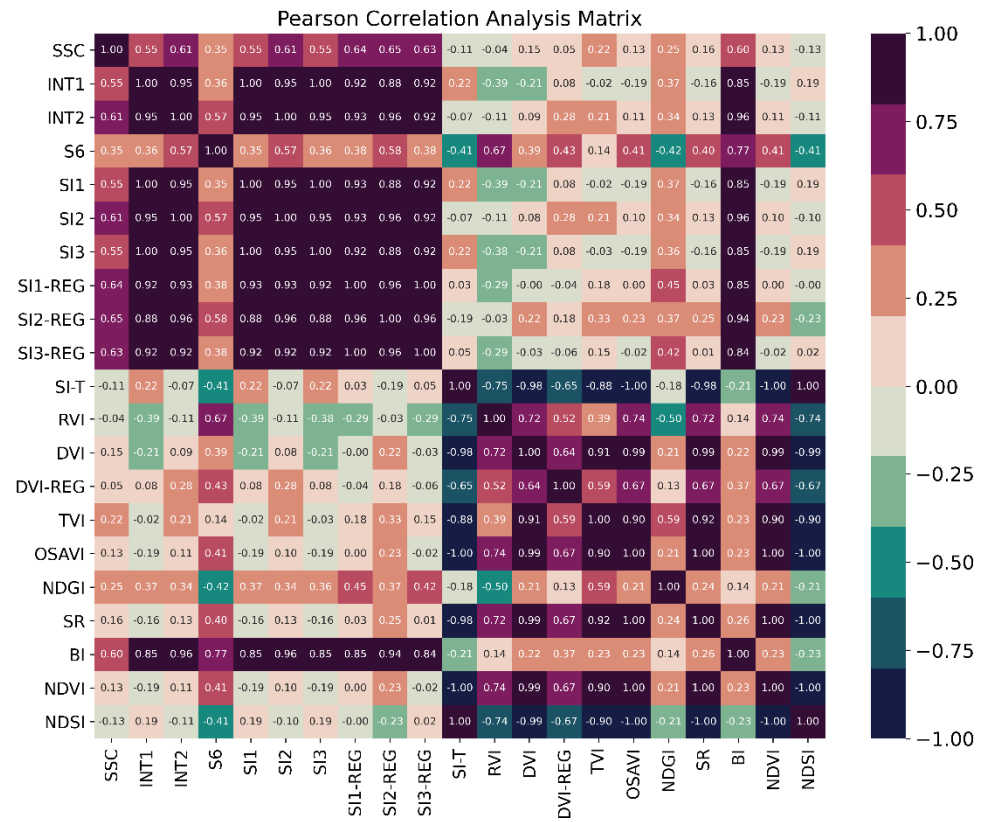


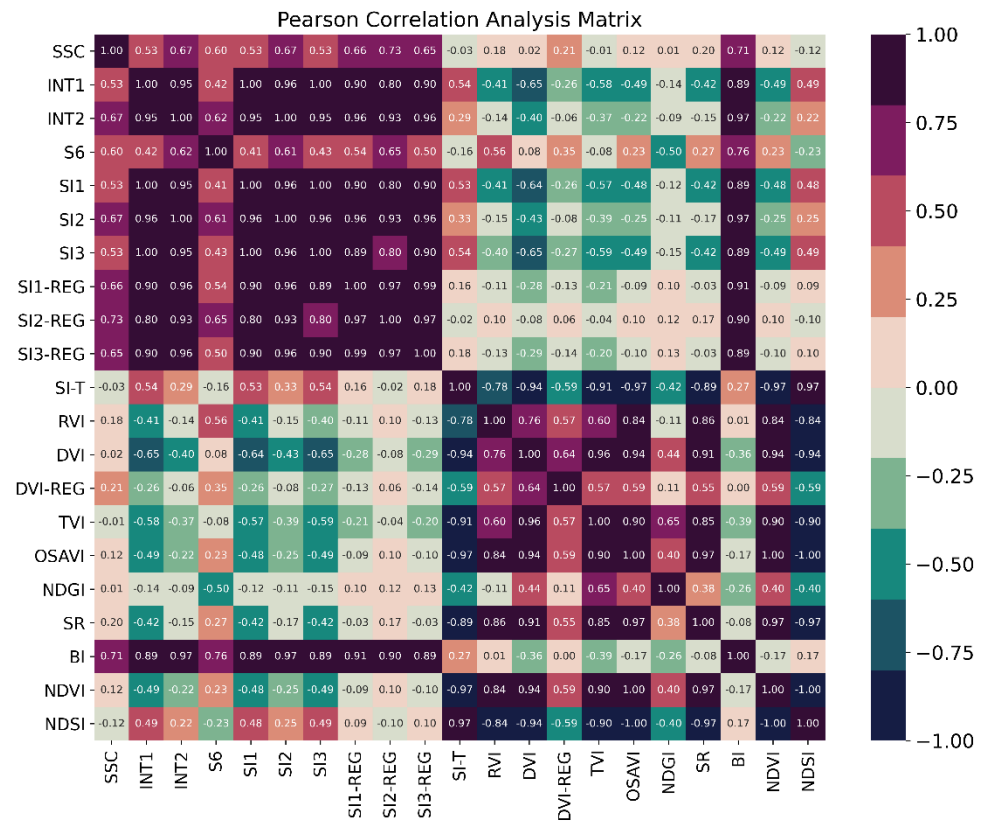
**Figure 4.** Correlations between soil salinity and spectral reflectance: (a) bare soil sample correlation; (b) vegetation area sample correlation.

#### 4.1.2. Sensitive Spectral Parameters

In order to improve the inversion accuracy of the model, we calculated some spectral indices and screened out the most highly sensitive indices as variables for modeling. As shown in Figure 5, among the 20 spectral indices calculated, those with correlations greater than 0.5, including INT1, INT2, SI1, SI2, SI3, SI1-R-edge, SI2-R-edge, SI3-R-edge, and BI, were selected for modeling.



(a)



(b)

**Figure 5.** Correlations between soil salinity and spectral index reflectance: (a) bare soil sample correlation; (b) vegetation area sample correlation.

#### 4.2. Soil Salinity Inversion Model Based on UAV Imagery

Based on the UAV imagery, the soil salinity inversion model was constructed by different regression methods using independent variables of characteristic bands, sensitive indices, and all characteristic spectral parameters. Tables 4 and 5 are the inversion results obtained by MLR, RF, SVM, and BPNN.

**Table 4.** Inversion results for the bare soil area.

Modeling Method	Variables	Modeling Accuracy			Validation Accuracy		
		$R^2$	RMSE (g/kg)	MAE (g/kg)	$R^2$	RMSE (g/kg)	MAE (g/kg)
MLR	band	0.5186	1.0027	0.7030	0.4327	1.1572	0.9301
	Spectral index	0.5432	1.0950	0.8125	0.4562	1.1086	0.8539
	All	0.6207	0.9872	0.7748	0.4478	1.1084	0.8565
RF	band	0.8498	0.5873	0.4207	0.7442	0.7848	0.7362
	Spectral index	0.8887	0.5100	0.3505	0.8540	0.4629	0.3301
	All	0.8924	0.5014	0.3602	0.8741	0.4298	0.3439
SVM	band	0.6947	0.8445	0.4783	0.6806	0.8496	0.0010
	Spectral index	0.6863	0.8562	0.4803	0.6828	0.8466	0.4406
	All	0.6897	0.8514	0.4789	0.6856	0.8769	0.4902
BPNN	band	0.6391	0.8483	0.5975	0.6177	1.0577	0.8346
	Spectral index	0.5144	1.1921	1.0242	0.5067	1.2015	1.0027
	All	0.5584	1.1368	0.9728	0.5543	1.1420	0.9800

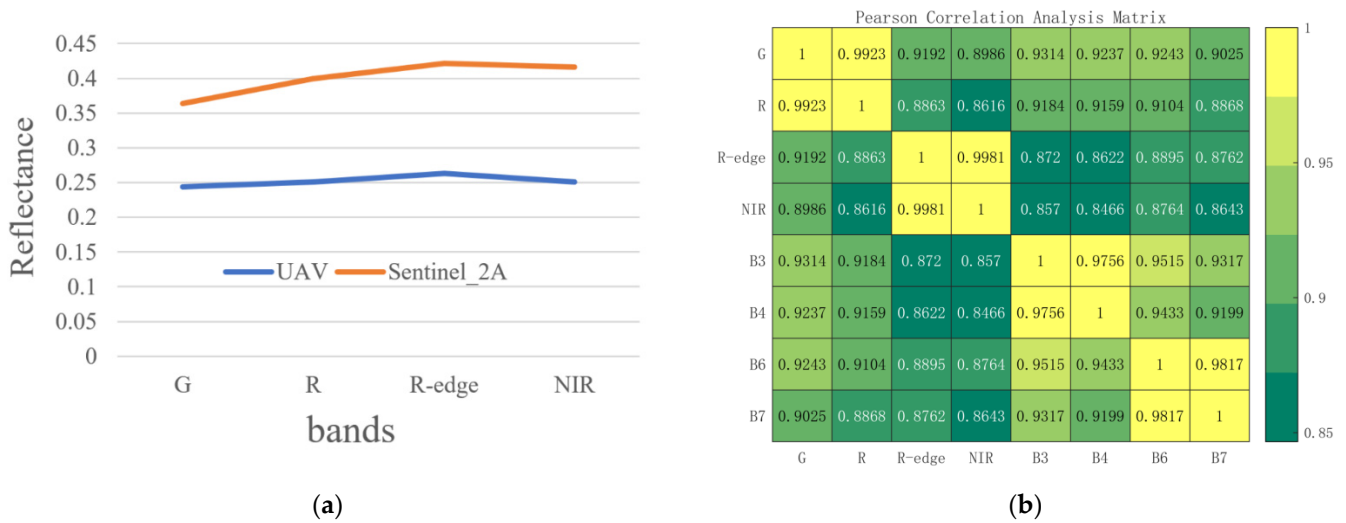
**Table 5.** Inversion results for the vegetation area.

Modeling Method	Variables	Modeling Accuracy			Validation Accuracy		
		$R^2$	RMSE (g/kg)	MAE (g/kg)	$R^2$	RMSE (g/kg)	MAE (g/kg)
MLR	band	0.5554	0.7737	0.6030	0.5603	0.7970	0.5956
	Spectral index	0.6140	0.5995	0.4290	0.6164	1.0613	0.7344
	All	0.7427	0.5983	0.4520	0.6244	0.6872	0.5583
RF	band	0.8753	0.3723	0.1673	0.7287	0.7917	0.3840
	Spectral index	0.8470	0.4728	0.2907	0.8082	0.4415	0.3142
	All	0.8990	0.3807	0.1949	0.7628	0.5120	0.3066
SVM	band	0.5898	0.7490	0.3049	0.5595	0.8343	0.3551
	Spectral index	0.5897	0.7491	0.3049	0.5730	0.7882	0.3273
	All	0.5898	0.7491	0.3049	0.5836	0.7565	0.3068
BPNN	band	0.7117	0.6532	0.4818	0.6630	0.5542	0.3495
	Spectral index	0.6205	0.7495	0.5744	0.5937	0.6084	0.4560
	All	0.6338	0.7362	0.5405	0.6011	0.6029	0.4413

In terms of modeling accuracy, the RF models significantly outperformed the other models, and the models with the full set of variables (sensitive bands and sensitive indices together as variables) significantly outperformed the models with only sensitive bands or sensitive indices. The results in Tables 4 and 5 show that the choice of model and variables has an important influence on the prediction of soil salinity. The modeling coefficient of determination ( $R^2$ ) of the best RF model in the bare soil area was 0.8741 with a RMSE of 0.4298 g/kg and a MAE of 0.3439 g/kg. The modeling coefficient of determination ( $R^2$ ) of the best RF model in the vegetated area was 0.8082 with a RMSE of 0.4415 g/kg and a MAE of 0.3142 g/kg.

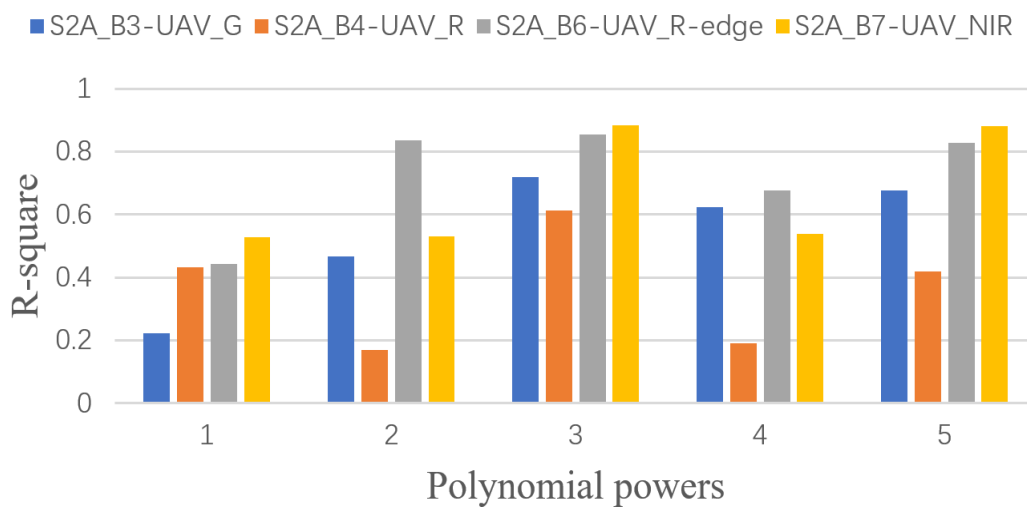
#### 4.3. Optimizing Sentinel-2A Reflectance Normalization Data

Figure 6 explores the relationship between the reflectivity of the UAV image and the Sentinel-2A image. Figure 6a shows that the surface reflectance of the UAV image was slightly higher than that of the Sentinel-2A image but that the trend of the two was extremely similar. Figure 6b shows that there was a strong correlation between the reflectivity of the UAV image and the satellite image band, indicating that it is indeed feasible to optimize the Sentinel-2A data based on the UAV data.



**Figure 6.** Correlations between UAV and Sentinel-2A: (a) trend of reflectance; (b) band correlation of UAV images and Sentinel-2A images.

We next used a polynomial fit function to explore the relationship between UAV data and sentinel data. Figure 7 shows our fitting results between similar bands for UAVs and satellites, where we see that the cubic polynomial had in the best fit for the data. Specifically, the G and B3 fit were 0.7177, the R and B4 fit were 0.6128, the R-edge and B6 fit were 0.8556, and the NIR and B7 fit were 0.8848.



**Figure 7.** Polynomial fitting results.

#### 4.4. Soil Salinity Inversion Model Based on Sentinel-2A Imagery

##### 4.4.1. Obtaining the Classification Mask

To obtain the soil area classification mask necessary for our model, we selected three classes of samples based on sentinel images, namely, vegetation, bare land, and water bodies, and classified them based on the supervised classification method (parallelepiped\ minimum distance\ mahalanobis distance\ minimum likelihood\ neural network\ support vector machine method) in the ENVI5.3 software. We used the overall precision (OA) and kappa coefficient to evaluate the classification results [44,45]. With Figures 8 and 9 we find that the support vector machine achieved the best classification results.

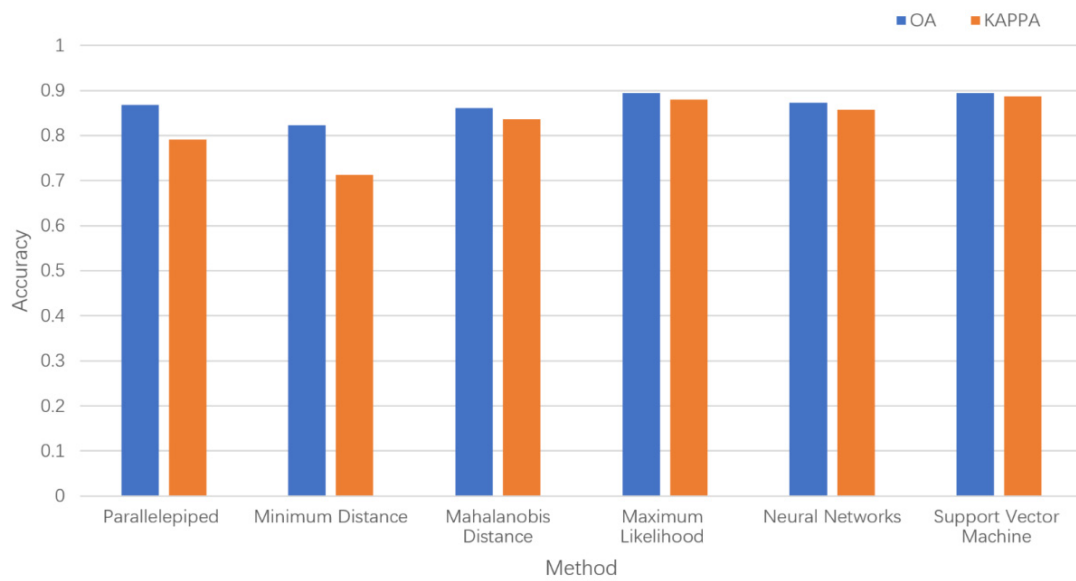


Figure 8. Classification accuracy of different methods.

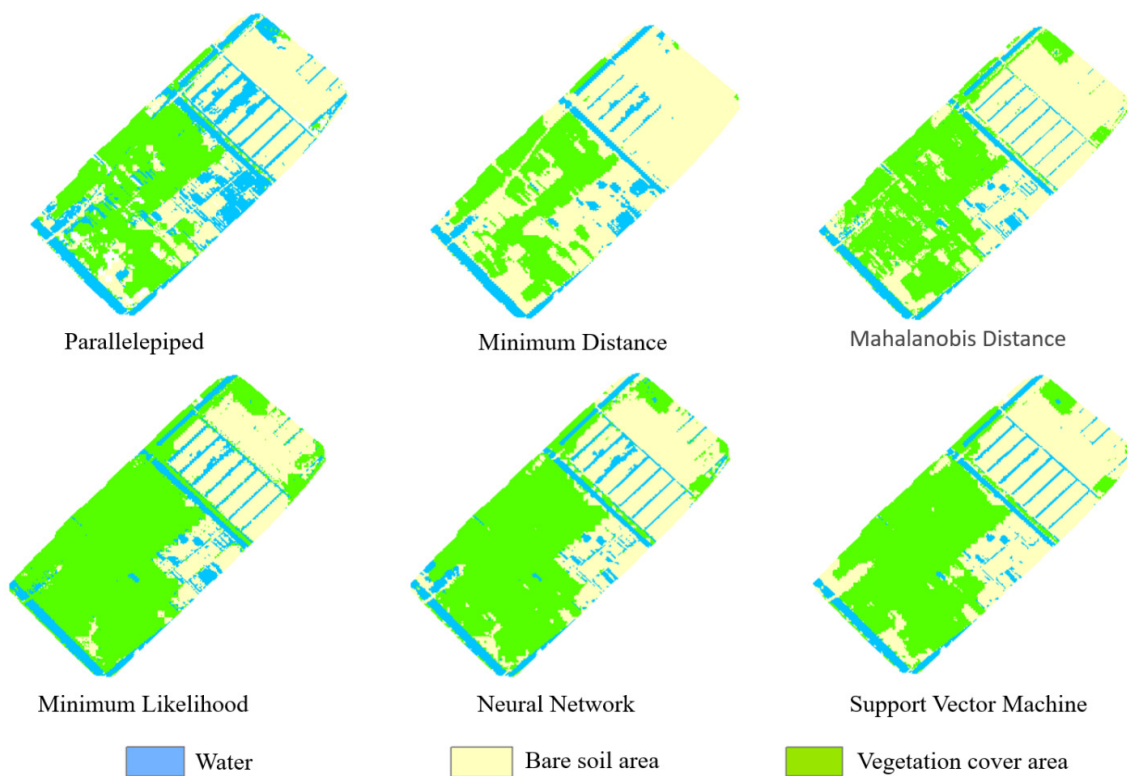


Figure 9. Visualization results of different classification methods.

The support vector machine classification results are shown in Table 6. Combined with the visualization results from Figure 9, we found that all three categories achieved good extraction results, allowing us to provide a basis for further improving the accuracy of satellite inversion of soil salinity.

Table 6. Category accuracy of support vector machine classification methods.

Method	Water	Bare Soil	Vegetation	Overall Accuracy	Kappa
SVM	0.8721	0.8932	0.8992	0.8942	0.8874

#### 4.4.2. Inversion and Validation in the Study Area

Table 7 shows the results obtained by using the best RF model established based on the UAV to perform the modeling inversion again on the satellite data. Modeling using only spectral bands in the bare soil area was superior to spectral indices and full variables. The modeling fit was 0.5758, the *RMSE* was 1.0105 g/kg, and the *MAE* was 0.6553 g/kg. Since the acquired variables were directly reflected by the ground surface, when some spectral indices were used for modeling, although they increased the diversity of data, it may have caused some data redundancy, resulting in a slightly lower fit than the model built using only bands. In the vegetation zone, the model with the full variables was better than the model with only spectral bands or spectral indices. Here the modeling fit was 0.6110, the *RMSE* was 0.6695 g/kg, and the *MAE* was 0.4607 g/kg. In this area, since the acquired spectral band values came from vegetation and not directly from the surface, some spectral indices may have been more helpful for modeling compared with spectral bands.

**Table 7.** Inversion results for satellite data.

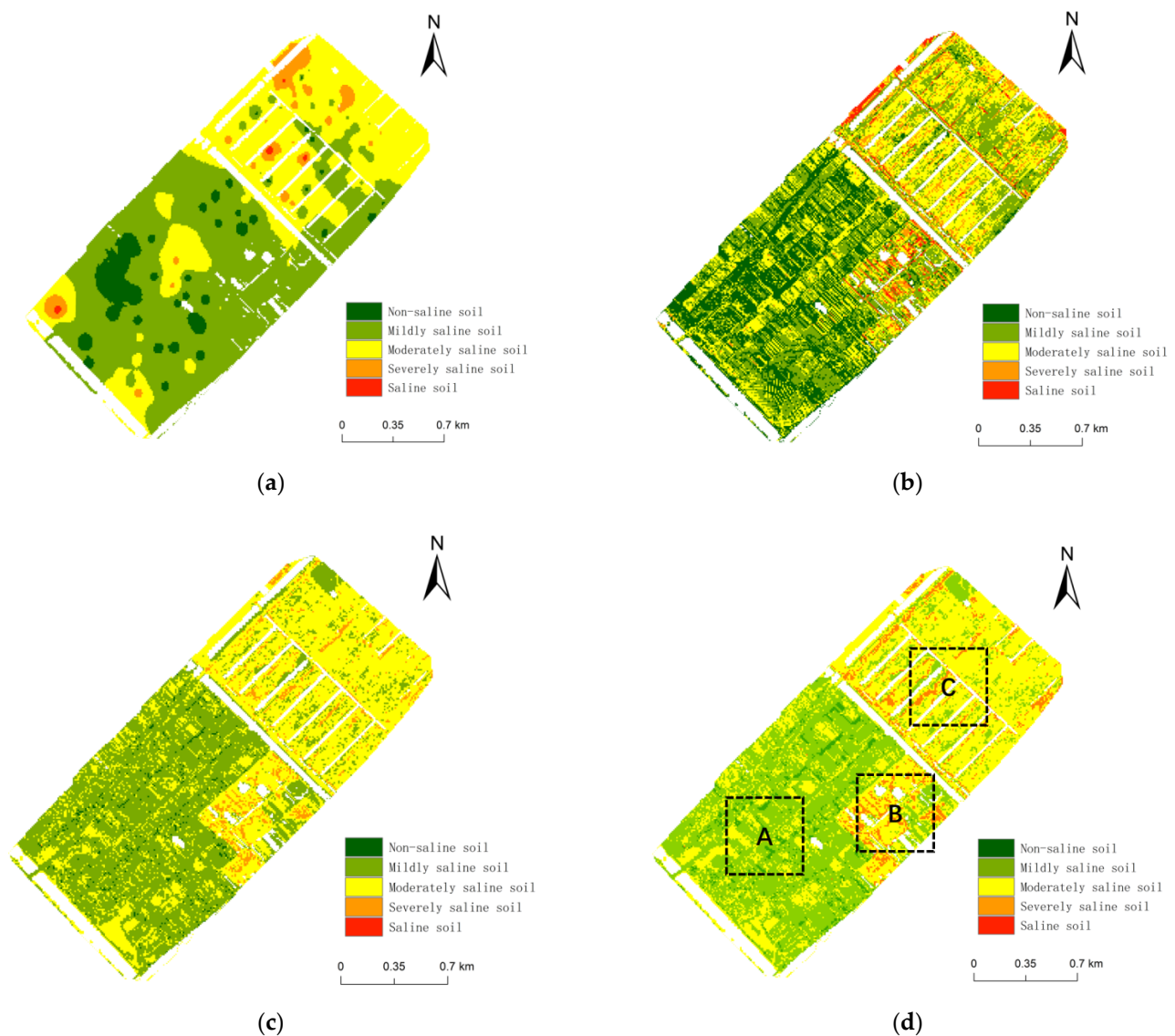
Study Area	Variables	Modeling Accuracy			Validation Accuracy		
		<i>R</i> <sup>2</sup>	<i>RMSE</i> (g/kg)	<i>MAE</i> (g/kg)	<i>R</i> <sup>2</sup>	<i>RMSE</i> (g/kg)	<i>MAE</i> (g/kg)
Bare soil area	band	0.6228	0.9388	0.6114	0.5758	1.0105	0.6553
	Spectral index	0.5947	0.9731	0.6324	0.5651	1.0787	0.6916
	All	0.6289	0.9312	0.5848	0.5631	1.3077	0.5456
Vegetation cover area	band	0.5875	0.7512	0.4424	0.5442	0.4427	0.3521
	Spectral index	0.6184	0.7225	0.4270	0.5554	1.0757	0.5830
	All	0.6204	0.7206	0.4707	0.6110	0.6695	0.4607

Table 8 shows the results obtained by re-modeling using the optimized satellite data. We can see that the accuracy of the modeling and inversion of the satellite data after polynomial fitting improved but was still slightly lower than the accuracy of the modeling using UAV data. The best fit for the bare soil area was 0.7702, with a *RMSE* of 0.63 g/kg and a *MAE* of 0.4751 g/kg. The best fit for the vegetated area was 0.6761, with a *RMSE* of 0.399 g/kg and a *MAE* of 0.2328 g/kg.

**Table 8.** Inversion results for optimizing satellite data based on drone data.

Study Area	Variables	Modeling Accuracy			Validation Accuracy		
		<i>R</i> <sup>2</sup>	<i>RMSE</i> (g/kg)	<i>MAE</i> (g/kg)	<i>R</i> <sup>2</sup>	<i>RMSE</i> (g/kg)	<i>MAE</i> (g/kg)
Bare soil area	band	0.7758	0.7238	0.5307	0.6314	0.9419	0.6632
	Spectral index	0.7838	0.7106	0.5599	0.7702	0.6300	0.4751
	All	0.7158	0.8148	0.5820	0.7345	0.7994	0.6275
Vegetation cover area	band	0.6850	0.6564	0.4368	0.6308	0.5801	0.3444
	Spectral index	0.7225	0.6160	0.3022	0.6761	0.3990	0.2328
	All	0.6154	0.7253	0.3964	0.6366	0.4423	0.2525

In general, in Figure 10a, the salinization of the area showed a gradual increase from south to north. Area C from Figure 10d belongs to the newly reclaimed area, and the soil salinity here is much higher than that of the surrounding soils. Furthermore, in contrast to the newly reclaimed bare ground, Area B is dry ponding. During the rainy season, heavy rain often washes away the salt on the surface, and the salt often accumulates in low-lying areas along with the rain. In area A, after years of reclamation and soil improvement, crops can already be planted in this area, so its salinity is not as serious as that of area C. From Table 9 we can see that the proportion of mild salinization soil and moderate salinization soil was largest at, 42.78% and 47.53%, respectively. The percentage of saline soil was the lowest at 1.12%.



**Figure 10.** Inversion results: (a) IDW interpolation map; (b) UAV inversion results; (c) Sentinel-2A inversion results; (d) inversion results for optimizing satellite data based on drone data.

**Table 9.** Percentage of salinized soil inversion results for optimizing satellite data based on drone data.

Soil Salinity Level	Non-Saline	Mild Salinization	Moderate Salinization	Severe Salinization	Saline Soil
Proportion of inversion result	3.21%	42.78%	47.53%	5.36%	1.12%

## 5. Discussion

Although our study was conducted during winter, some vegetation was still growing in January due to the northern subtropical monsoon climate of the bay. In order to accurately invert the soil salt content in bare soil and vegetated areas, we adopted a classification first and then inversion approach. Compared with the traditional soil salinity model, the soil salinity model based on zonal inversion can provide more accurate inversion results. Through Table 8, we can see that the model built in the bare soil area was better than the model built in the vegetated area. This may be due to the fact that the vegetation cover is not uniform due to the season, resulting in a small amount of bare soil areas that affect the model building. However, this justifies the need of zonal sampling for classification

inversion. Since different vegetation types have different stresses on soil salinity [46–48], in order to further eliminate the interference caused by different vegetation types on the inversion, we can further classify them and reduce or eliminate this effect by fine class division [49]. The study date in this paper was in winter, when vegetation types were sparse and homogeneous, and we did not reclassify vegetation types in the vegetation zone. For this reason, in our future research we will increase our efforts to study soil salinity inversion in areas with different types of vegetation to establish a more robust modeling approach.

To explore the effects of different spectra with corresponding spectral indices on soil salinity, we first used correlation analysis to measure whether these spectral variables are closely correlated with soil salinity. As shown in Figure 3, the correlation between R-edge and NIR bands and soil salinity was relatively high, which is consistent with previous studies [50,51]. However direct monitoring of very slight and minor salinity using multispectral images is limited because different soil salinities have different spectral properties [52–54]. For this reason, we further used the relevant spectral indices as model covariates to invert surface salinity. As in the inversion of soil salinity in vegetated areas, different degrees of salinization can stress the growth of vegetation, which is more sensitive to soil salinity stress. Therefore, soil salinity and its trend can be indirectly inferred from the vegetation index [38]. Sidike et al. also indicated that the spectral covariates Int1 and Int2, and soil salinity indices SI1, SI2, and SI3 are sensitive to soil salinity and contribute to the accuracy of soil salinity mapping [55]. In our inversion of salinity in the coastal plain, the salt index was always better than the vegetation index. This indicates that the salinity index is more sensitive to the response of soil salinity [10,56–58]. Therefore, when selecting the best remote sensing index for soil salinity estimation, multi-band remote sensing data are used as variables to enhance the sensitivity of inversion variables to soil salinity information by combining different band operations [57,59,60].

Not all spectral variables contribute to soil salinity estimation, and their importance needs to be evaluated to determine the optimal inversion variables; too many variables also cause data redundancy, resulting in the consumption of computational resources and model instability [61]. In this study, we initially selected inversion variables by setting thresholds based on Pearson correlation analysis. Although complete spectral variables can represent the soil salinity characteristics as much as possible, too many variables will inevitably cause data redundancy and reduce the efficiency of the calculation [62]. In our experimental result (Table 5), based on the inversion model of random forest, we can see that the robustness of the model was reduced when the model was applied in the testing phase because spectral variables of the same nature were not excluded, resulting in data redundancy, despite the optimal fit achieved at the time of model building. Therefore, in future studies we will choose more environmental variables and adopt corresponding data redundancy elimination methods in order to build more robust models.

Ground truth data are the basis for quantitative soil analysis, UAV near earth remote sensing is the link between satellites and the ground, and satellite remote sensing is the platform for large area inversion. Combining the three is on track to become an important way to obtain soil salt information at present and in the future [32]. As shown in Table 7, the model constructed based on Sentinel-2A data obtained worse results on three different inversion covariates than the results obtained based on UAV inversion. Although the satellite images cover a large area, their spatial information is coarse, which often limits the accurate interpretation of soil attributes. For this reason, we first found the most sensitive parameters corresponding to soil salinity in the region based on high-spatial-resolution UAV images, and then built models on different ground covers to lay the foundation for large-scale soil salinity inversion by satellite. To improve the sensitivity of satellite data to soil covariates, we also further optimized the Sentinel-2A data. As shown in Figure 7, we constructed polynomials of order 1 to 5 to explore the optimal correction equation according to the mutual corresponding bands of the UAV and satellite in order to find a robust optimization equation. The next step is to continue to explore the linkage between

UAV and satellite data and establish a more robust data optimization method to achieve even more accurate salt distribution mapping on a large scale.

## 6. Conclusions

In this paper, we explored high-precision and large-scale inversion methods for soil salinity based on UAV and satellite data from a coastal area of eastern China. Our analysis was based on the feasibility of modeling soil salinity with sensitive bands and sensitive indices of UAV images. After experimental validation among the research methods used in this paper, we found that RF had the best fit, reaching 87.41% in bare soil area and 80.82% in vegetated area, which are both high enough to perform soil salinity mapping in practice. To meet the need for large-scale soil salinity mapping, we also explored the relationship between UAV images and satellite images and found that there was a strong correlation between their corresponding bands. From this, we used a polynomial fitting method based on UAV data to optimize the satellite data and invert the images by partition to improve the accuracy of large-scale soil salinity mapping. The final results showed that our method can effectively improve satellite-based large-scale salt inversion.

However, there are still three important aspects of this area of research that have not been explored more deeply. First, the correlation between the selection or construction of model inversion parameters and the corresponding soil salinity in the study area need to be further explored. Second, the construction of inversion models, such as deep learning and other methods with powerful feature characterization capabilities can be used to enhance inversion accuracy. Finally, we did not deeply explore the connection between UAV and satellite data to establish a more robust data optimization method capable of achieving even more accurate salt distribution mapping on a large scale.

**Author Contributions:** Conceptualization, L.X. and X.F.; methodology, L.X.; software, L.X.; validation, C.Z., Y.D. and J.C.; formal analysis, X.F.; investigation, C.Z.; resources, X.F.; data curation, L.X.; writing—original draft preparation, L.X.; writing—review and editing, X.F.; visualization, J.H.; supervision, J.H. All authors have read and agreed to the published version of the manuscript.

**Funding:** National Natural Science Foundation of China (41976209).

**Institutional Review Board Statement:** Not applicable.

**Informed Consent Statement:** Not applicable.

**Data Availability Statement:** Not applicable.

**Acknowledgments:** The authors would like to give our sincerest thanks to the anonymous reviewers for their constructive suggestions and comments, which are of great value for improving the manuscript. The authors also thank the Editor for the kind assistances and beneficial comments. The authors are grateful for the kind support from the editorial office.

**Conflicts of Interest:** The authors declare no conflict of interest.

## References

1. Jiang, Q.; Peng, J.; Biswas, A.; Hu, J.; Zhao, R.; He, K.; Shi, Z. Characterising dryland salinity in three dimensions. *Sci. Total Environ.* **2019**, *682*, 190–199. [[CrossRef](#)] [[PubMed](#)]
2. Aldabaa, A.A.A.; Weindorf, D.C.; Chakraborty, S.; Sharma, A.; Li, B. Combination of proximal and remote sensing methods for rapid soil salinity quantification. *Geoderma* **2015**, *239–240*, 34–46. [[CrossRef](#)]
3. Mukhopadhyay, R.; Sarkar, B.; Jat, H.S.; Sharma, P.C.; Bolan, N.S. Soil salinity under climate change: Challenges for sustainable agriculture and food security. *J. Environ. Manag.* **2021**, *280*, 111736. [[CrossRef](#)] [[PubMed](#)]
4. Sahab, S.; Suhani, I.; Srivastava, V.; Chauhan, P.S.; Singh, R.P.; Prasad, V. Potential risk assessment of soil salinity to agroecosystem sustainability: Current status and management strategies. *Sci. Total Environ.* **2021**, *764*, 144164. [[CrossRef](#)] [[PubMed](#)]
5. Abbas, A.; Khan, S.; Hussain, N.; Hanjra, M.A.; Akbar, S. Characterizing soil salinity in irrigated agriculture using a remote sensing approach. *Phys. Chem. Earth Parts A/B/C* **2013**, *55–57*, 43–52. [[CrossRef](#)]
6. Gorji, T.; Tanik, A.; Sertel, E. Soil Salinity Prediction, Monitoring and Mapping Using Modern Technologies. *Procedia Earth Planet. Sci.* **2015**, *15*, 507–512. [[CrossRef](#)]
7. Pan, X.; Chen, Y.; Cui, J.; Peng, Z.; Fu, X.; Wang, Y.; Men, M. Accuracy analysis of remote sensing index enhancement for SVM salt inversion model. *Geocarto Int.* **2021**, *37*, 2406–2423. [[CrossRef](#)]

8. Rossel, R.A.V.; Webster, R. Predicting soil properties from the Australian soil visible-near infrared spectroscopic database. *Eur. J. Soil Sci.* **2012**, *63*, 848–860. [[CrossRef](#)]
9. Abdullah, A.Y.M.; Biswas, R.K.; Chowdhury, A.I.; Billah, S.M. Modeling soil salinity using direct and indirect measurement techniques: A comparative analysis. *Environ. Dev.* **2019**, *29*, 67–80. [[CrossRef](#)]
10. Nouri, H.; Chavoshi Borujeni, S.; Alaghmand, S.; Anderson, S.; Sutton, P.; Parvazian, S.; Beecham, S. Soil Salinity Mapping of Urban Greenery Using Remote Sensing and Proximal Sensing Techniques; The Case of Veale Gardens within the Adelaide Parklands. *Sustainability* **2018**, *10*, 2826. [[CrossRef](#)]
11. Meng, B.; Ge, J.; Liang, T.; Yang, S.; Gao, J.; Feng, Q.; Cui, X.; Huang, X.; Xie, H. Evaluation of Remote Sensing Inversion Error for the Above-Ground Biomass of Alpine Meadow Grassland Based on Multi-Source Satellite Data. *Remote Sens.* **2017**, *9*, 372. [[CrossRef](#)]
12. Shi, H.; Hellwich, O.; Luo, G.; Chen, C.; He, H.; Ochege, F.U.; Van de Voorde, T.; Kurban, A.; Maeyer, P.d. A Global Meta-Analysis of Soil Salinity Prediction Integrating Satellite Remote Sensing, Soil Sampling, and Machine Learning. *IEEE Trans. Geosci. Remote Sens.* **2022**, *60*, 1–15. [[CrossRef](#)]
13. Zhang, S.; Zhao, G. A Harmonious Satellite-Unmanned Aerial Vehicle-Ground Measurement Inversion Method for Monitoring Salinity in Coastal Saline Soil. *Remote Sens.* **2019**, *11*, 1700. [[CrossRef](#)]
14. Zhang, H.; Wang, L.; Tian, T.; Yin, J. A Review of Unmanned Aerial Vehicle Low-Altitude Remote Sensing (UAV-LARS) Use in Agricultural Monitoring in China. *Remote Sens.* **2021**, *13*, 1221. [[CrossRef](#)]
15. Wang, D.; Shao, Q.; Yue, H. Surveying Wild Animals from Satellites, Manned Aircraft and Unmanned Aerial Systems (UASs): A Review. *Remote Sens.* **2019**, *11*, 1308. [[CrossRef](#)]
16. Otsu, K.; Pla, M.; Vayreda, J.; Brotons, L. Calibrating the Severity of Forest Defoliation by Pine Processionary Moth with Landsat and UAV Imagery. *Sensors* **2018**, *18*, 3278. [[CrossRef](#)] [[PubMed](#)]
17. Dong, R.; Na, X. Quantitative Retrieval of Soil Salinity Using Landsat 8 OLI Imagery. *Appl. Sci.* **2021**, *11*, 11145. [[CrossRef](#)]
18. Peng, J.; Biswas, A.; Jiang, Q.; Zhao, R.; Hu, J.; Hu, B.; Shi, Z. Estimating soil salinity from remote sensing and terrain data in southern Xinjiang Province, China. *Geoderma* **2019**, *337*, 1309–1319. [[CrossRef](#)]
19. Maimaitijiang, M.; Sagan, V.; Sidike, P.; Daloye, A.M.; Erkbol, H.; Fritschi, F.B. Crop Monitoring Using Satellite/UAV Data Fusion and Machine Learning. *Remote Sens.* **2020**, *12*, 1357. [[CrossRef](#)]
20. Tian, P.; Li, J.; Cao, L.; Pu, R.; Gong, H.; Liu, Y.; Zhang, H.; Chen, H. Impacts of reclamation derived land use changes on ecosystem services in a typical gulf of eastern China: A case study of Hangzhou bay. *Ecol. Indic.* **2021**, *132*, 108259. [[CrossRef](#)]
21. Zhang, D.; Jia, G.; Chen, L.; Jin, H.; Wang, Z.; Feng, W.; Zhang, Y. Seasonal succession and spatial heterogeneity of the nekton community associated with environmental factors in Hangzhou Bay, China. *Reg. Stud. Mar. Sci.* **2022**, *49*, 102108. [[CrossRef](#)]
22. Qiu, L.; Zhang, M.; Zhou, B.; Cui, Y.; Yu, Z.; Liu, T.; Wu, S. Economic and ecological trade-offs of coastal reclamation in the Hangzhou Bay, China. *Ecol. Indic.* **2021**, *125*, 107477. [[CrossRef](#)]
23. Muhetaer, N.; Nurmemet, I.; Abulaiti, A.; Xiao, S.; Zhao, J. A Quantifying Approach to Soil Salinity Based on a Radar Feature Space Model Using ALOS PALSAR-2 Data. *Remote Sens.* **2022**, *14*, 363. [[CrossRef](#)]
24. Wang, Z.; Zhao, G.; Gao, M.; Chang, C. Spatial variability of soil salinity in coastal saline soil at different scales in the Yellow River Delta, China. *Environ. Monit. Assess.* **2017**, *189*, 80. [[CrossRef](#)] [[PubMed](#)]
25. Bao, S.D. *Soil Agrochemical Analysis*; China Agriculture Press: Beijing, China, 2000; Volume 30.
26. Miura, T.; Huete, A.; Yoshioka, H. An empirical investigation of cross-sensor relationships of NDVI and red/near-infrared reflectance using EO-1 Hyperion data. *Remote Sens. Environ.* **2006**, *100*, 223–236. [[CrossRef](#)]
27. Ma, Y.; Chen, H.; Zhao, G.; Wang, Z.; Wang, D. Spectral Index Fusion for Salinized Soil Salinity Inversion Using Sentinel-2A and UAV Images in a Coastal Area. *IEEE Access* **2020**, *8*, 159595–159608. [[CrossRef](#)]
28. Douaoui, A.E.K.; Nicolas, H.; Walter, C. Detecting salinity hazards within a semiarid context by means of combining soil and remote-sensing data. *Geoderma* **2006**, *134*, 217–230. [[CrossRef](#)]
29. Triki Fourati, H.; Bouaziz, M.; Benzina, M.; Bouaziz, S. Modeling of soil salinity within a semi-arid region using spectral analysis. *Arab. J. Geosci.* **2015**, *8*, 11175–11182. [[CrossRef](#)]
30. Wang, J.; Ding, J.; Yu, D.; Ma, X.; Zhang, Z.; Ge, X.; Teng, D.; Li, X.; Liang, J.; Lizaga, I.; et al. Capability of Sentinel-2 MSI data for monitoring and mapping of soil salinity in dry and wet seasons in the Ebinur Lake region, Xinjiang, China. *Geoderma* **2019**, *353*, 172–187. [[CrossRef](#)]
31. Zhang, S.; Zhao, G.; Lang, K.; Su, B.; Chen, X.; Xi, X.; Zhang, H. Integrated Satellite, Unmanned Aerial Vehicle (UAV) and Ground Inversion of the SPAD of Winter Wheat in the Reviving Stage. *Sensors* **2019**, *19*, 1485. [[CrossRef](#)]
32. Qi, G.; Zhao, G.; Xi, X. Soil Salinity Inversion of Winter Wheat Areas Based on Satellite-Unmanned Aerial Vehicle-Ground Collaborative System in Coastal of the Yellow River Delta. *Sensors* **2020**, *20*, 6521. [[CrossRef](#)] [[PubMed](#)]
33. Al-Gaadi, K.A.; Tola, E.; Madugundu, R.; Fulleros, R.B.C.S. Sentinel-2 images for effective mapping of soil salinity in agricultural fields. *Curr. Sci.* **2021**, *121*, 384–390. [[CrossRef](#)]
34. Allbed, A.; Kumar, L.; Aldakheel, Y.Y. Assessing soil salinity using soil salinity and vegetation indices derived from IKONOS high-spatial resolution imageries: Applications in a date palm dominated region. *Geoderma* **2014**, *230–231*, 1–8. [[CrossRef](#)]
35. Zhu, W.; Rezaei, E.E.; Nouri, H.; Yang, T.; Li, B.; Gong, H.; Lyu, Y.; Peng, J.; Sun, Z. Quick Detection of Field-Scale Soil Comprehensive Attributes via the Integration of UAV and Sentinel-2B Remote Sensing Data. *Remote Sens.* **2021**, *13*, 4716. [[CrossRef](#)]

36. Khan, N.M.; Rastoskuev, V.V.; Sato, Y.; Shiozawa, S. Assessment of hydrosaline land degradation by using a simple approach of remote sensing indicators. *Agric. Water Manag.* **2005**, *77*, 96–109. [[CrossRef](#)]
37. Yin, L.; Zhang, H.; Zhou, X.; Yuan, X.; Zhao, S.; Li, X.; Liu, X. KAML: Improving genomic prediction accuracy of complex traits using machine learning determined parameters. *Genome Biol.* **2020**, *21*, 146. [[CrossRef](#)]
38. Ma, G.; Ding, J.; Han, L.; Zhang, Z.; Ran, S. Digital mapping of soil salinization based on Sentinel-1 and Sentinel-2 data combined with machine learning algorithms. *Reg. Sustain.* **2021**, *2*, 177–188. [[CrossRef](#)]
39. Zhu, C.; Ding, J.; Zhang, Z.; Wang, J.; Wang, Z.; Chen, X.; Wang, J. SPAD monitoring of saline vegetation based on Gaussian mixture model and UAV hyperspectral image feature classification. *Comput. Electron. Agric.* **2022**, *200*, 107236. [[CrossRef](#)]
40. Chen, H.; Ma, Y.; Zhu, A.; Wang, Z.; Zhao, G.; Wei, Y. Soil salinity inversion based on differentiated fusion of satellite image and ground spectra. *Int. J. Appl. Earth Obs. Geoinf.* **2021**, *101*, 102360. [[CrossRef](#)]
41. Wang, J.; Wang, W.; Hu, Y.; Tian, S.; Liu, D. Soil Moisture and Salinity Inversion Based on New Remote Sensing Index and Neural Network at a Salina-Alkaline Wetland. *Water* **2021**, *13*, 2762. [[CrossRef](#)]
42. Yu, X.; Chang, C.; Song, J.; Zhuge, Y.; Wang, A. Precise Monitoring of Soil Salinity in China's Yellow River Delta Using UAV-Borne Multispectral Imagery and a Soil Salinity Retrieval Index. *Sensors* **2022**, *22*, 546. [[CrossRef](#)] [[PubMed](#)]
43. Alvarez-Vanhard, E.; Corpetti, T.; Houet, T. UAV & satellite synergies for optical remote sensing applications: A literature review. *Sci. Remote Sens.* **2021**, *3*, 100019. [[CrossRef](#)]
44. Zhang, C.; Li, G.; Lei, R.; Du, S.; Zhang, X.; Zheng, H.; Wu, Z. Deep Feature Aggregation Network for Hyperspectral Remote Sensing Image Classification. *IEEE J. Sel. Top. Appl. Earth Obs. Remote Sens.* **2020**, *13*, 5314–5325. [[CrossRef](#)]
45. Li, S.; Song, W.; Fang, L.; Chen, Y.; Ghamisi, P.; Benediktsson, J.A. Deep Learning for Hyperspectral Image Classification: An Overview. *IEEE Trans. Geosci. Remote Sens.* **2019**, *57*, 6690–6709. [[CrossRef](#)]
46. Yu, Z.; Duan, X.; Luo, L.; Dai, S.; Ding, Z.; Xia, G. How Plant Hormones Mediate Salt Stress Responses. *Trends Plant Sci.* **2020**, *25*, 1117–1130. [[CrossRef](#)]
47. El Moukhtari, A.; Cabassa-Hourton, C.; Farissi, M.; Savoure, A. How Does Proline Treatment Promote Salt Stress Tolerance During Crop Plant Development? *Front. Plant Sci.* **2020**, *11*, 1127. [[CrossRef](#)] [[PubMed](#)]
48. Zhao, S.; Zhang, Q.; Liu, M.; Zhou, H.; Ma, C.; Wang, P. Regulation of Plant Responses to Salt Stress. *Int. J. Mol. Sci.* **2021**, *22*, 4609. [[CrossRef](#)] [[PubMed](#)]
49. Wu, W.; Al-Shafie, W.M.; Mhaimeed, A.S.; Ziadat, F.; Nangia, V.; Payne, W.B. Soil Salinity Mapping by Multiscale Remote Sensing in Mesopotamia, Iraq. *IEEE J. Sel. Top. Appl. Earth Obs. Remote Sens.* **2014**, *7*, 4442–4452. [[CrossRef](#)]
50. Zhu, W.; Sun, Z.; Yang, T.; Li, J.; Peng, J.; Zhu, K.; Li, S.; Gong, H.; Lyu, Y.; Li, B.; et al. Estimating leaf chlorophyll content of crops via optimal unmanned aerial vehicle hyperspectral data at multi-scales. *Comput. Electron. Agric.* **2020**, *178*, 105786. [[CrossRef](#)]
51. Dong, T.; Liu, J.; Shang, J.; Qian, B.; Ma, B.; Kovacs, J.M.; Walters, D.; Jiao, X.; Geng, X.; Shi, Y. Assessment of red-edge vegetation indices for crop leaf area index estimation. *Remote Sens. Environ.* **2019**, *222*, 133–143. [[CrossRef](#)]
52. Fan, X.; Weng, Y.; Tao, J. Towards decadal soil salinity mapping using Landsat time series data. *Int. J. Appl. Earth Obs. Geoinf.* **2016**, *52*, 32–41. [[CrossRef](#)]
53. Masoud, A.A.; Koike, K.; Atwia, M.G.; El-Horiny, M.M.; Gemail, K.S. Mapping soil salinity using spectral mixture analysis of landsat 8 OLI images to identify factors influencing salinization in an arid region. *Int. J. Appl. Earth Obs. Geoinf.* **2019**, *83*, 101944. [[CrossRef](#)]
54. Ge, X.; Ding, J.; Teng, D.; Xie, B.; Zhang, X.; Wang, J.; Han, L.; Bao, Q.; Wang, J. Exploring the capability of Gaofen-5 hyperspectral data for assessing soil salinity risks. *Int. J. Appl. Earth Obs. Geoinf.* **2022**, *112*, 102969. [[CrossRef](#)]
55. Sidike, A.; Zhao, S.; Wen, Y. Estimating soil salinity in Pingluo County of China using QuickBird data and soil reflectance spectra. *Int. J. Appl. Earth Obs. Geoinf.* **2014**, *26*, 156–175. [[CrossRef](#)]
56. Elhag, M.; Bahrawi, J.A. Soil salinity mapping and hydrological drought indices assessment in arid environments based on remote sensing techniques. *Geosci. Instrum. Methods Data Syst.* **2017**, *6*, 149–158. [[CrossRef](#)]
57. Wang, X.; Zhang, F.; Ding, J.; Kung, H.T.; Latif, A.; Johnson, V.C. Estimation of soil salt content (SSC) in the Ebinur Lake Wetland National Nature Reserve (ELWNNR), Northwest China, based on a Bootstrap-BP neural network model and optimal spectral indices. *Sci. Total Environ.* **2018**, *615*, 918–930. [[CrossRef](#)]
58. Deng, L.; Mao, Z.; Li, X.; Hu, Z.; Duan, F.; Yan, Y. UAV-based multispectral remote sensing for precision agriculture: A comparison between different cameras. *ISPRS J. Photogramm. Remote Sens.* **2018**, *146*, 124–136. [[CrossRef](#)]
59. Farifteh, J.; Farshad, A.; George, R.J. Assessing salt-affected soils using remote sensing, solute modelling, and geophysics. *Geoderma* **2006**, *130*, 191–206. [[CrossRef](#)]
60. Fernández-Buces, N.; Siebe, C.; Cram, S.; Palacio, J.L. Mapping soil salinity using a combined spectral response index for bare soil and vegetation: A case study in the former lake Texcoco, Mexico. *J. Arid Environ.* **2006**, *65*, 644–667. [[CrossRef](#)]
61. Ge, X.; Ding, J.; Teng, D.; Wang, J.; Huo, T.; Jin, X.; Wang, J.; He, B.; Han, L. Updated soil salinity with fine spatial resolution and high accuracy: The synergy of Sentinel-2 MSI, environmental covariates and hybrid machine learning approaches. *Catena* **2022**, *212*, 106054. [[CrossRef](#)]
62. Wang, F.; Shi, Z.; Biswas, A.; Yang, S.; Ding, J. Multi-algorithm comparison for predicting soil salinity. *Geoderma* **2020**, *365*, 114211. [[CrossRef](#)]